

8-9-2022

The Fermilab SpinQuest Experiment: Commissioning and plans toward production

Nuwan Chaminda Gunawardhana Waduge
Mississippi State University, mra2mh@virginia.edu

Follow this and additional works at: <https://scholarsjunction.msstate.edu/td>



Part of the [Nuclear Commons](#)

Recommended Citation

Gunawardhana Waduge, Nuwan Chaminda, "The Fermilab SpinQuest Experiment: Commissioning and plans toward production" (2022). *Theses and Dissertations*. 5536.
<https://scholarsjunction.msstate.edu/td/5536>

This Graduate Thesis - Open Access is brought to you for free and open access by the Theses and Dissertations at Scholars Junction. It has been accepted for inclusion in Theses and Dissertations by an authorized administrator of Scholars Junction. For more information, please contact scholcomm@msstate.libanswers.com.

The Fermilab SpinQuest Experiment: Commissioning and plans toward production

By

GW Nuwan Chaminda

Approved by:

Lamiaa El Fassi (Major Professor)
Dipangkar Dutta
Kenichi Nakano
Hendrick F. Arnoldus (Graduate Coordinator)
Rick Travis (Dean, College of Arts & Sciences)

A Thesis
Submitted to the Faculty of
Mississippi State University
in Partial Fulfillment of the Requirements
for the Degree of Master of Science
in Physics
in the Department of Physics and Astronomy

Mississippi State, Mississippi

August 2022

Copyright by
GW Nuwan Chaminda
2022

Name: GW Nuwan Chaminda

Date of Degree: August 9, 2022

Institution: Mississippi State University

Major Field: Physics

Major Professor: Lamiaa El Fassi

Title of Study: The Fermilab SpinQuest Experiment: Commissioning and plans toward production

Pages in Study: 54

Candidate for Degree of Master of Science

E1039/SpinQuest, a transversely-polarized Drell-Yan experiment at Fermilab, plans to use the 120 GeV proton beam and polarized NH₃ and ND₃ cryogenic targets to study azimuthal asymmetries in dimuon production to extract the magnitude as well as sign of the sea quarks *Sivers* functions. The SpinQuest spectrometer is optimized to detect oppositely-charged muons with a series of tracking chambers and hodoscope stations. The scope of this manuscript is to highlight the physics goals and the experimental setup with a focus on the ongoing debugging and training of one of the tracking systems, mainly drift chambers, as preparation for the upcoming commissioning and production run-periods.

This work is supported in part by the US DOE contract number DE-FG02-07ER41528.

Key words: Drell-Yan, Fermilab, SpinQuest, Polarization, Tracking, Drift Chambers

DEDICATION

To my mom.

ACKNOWLEDGEMENTS

I would like to first acknowledge the SpinQuest collaboration at Fermilab who made this work possible. Many of the collaborators who worked with me at NM4 have been my mentors and I am grateful for the support provided by Dustin Keller, Kun Liu, Kenichi Nakano, Kei Nagai, and Rick Tesarek. I would also like to thank everyone who helped me accessing NM4 experimental hall, and everyone who always helped me at the work.

My advisor, Prof. Lamiaa El Fassi has been the main support and inspiration behind this work. She helped immensely in writing the thesis and guided me in completing my work at this project. I highly appreciate all the advice she provided.

My family, especially my mom, my grandmother, my life partner Dulanji Kariyawasam and my friends have been my strength during hard times. I would like to thank them for their prayers and all strength they provided me.

Last but not least, I would like to acknowledge my thesis M.S. committee members for assisting with my defense evaluation and for providing valuable comments while reviewing this manuscript.

TABLE OF CONTENTS

DEDICATION	ii
ACKNOWLEDGEMENTS	iii
LIST OF TABLES	vi
LIST OF FIGURES	vii
LIST OF SYMBOLS, ABBREVIATIONS, AND NOMENCLATURE	x
CHAPTER	
I. INTRODUCTION	1
1.1 SpinQuest Motivation.....	1
1.2 First-publication Physics Goals	2
II. EXPERIMENTAL SETUP	6
2.2 Beam.....	8
2.3 Target.....	9
2.4 Magnets	9
2.5 Hodoscopes.....	10
2.6 Drift Chambers	11
2.7 Proportional Tubes	14
2.8 Trigger	14
2.9 Data Acquisition.....	14
III. DRIFT CHAMBER REPAIR AND DEBUGGING	16
3.1 Problematic Hit Distributions Channels	16
3.2 Drift Chambers Repair	22
3.2.1 St-1 D0XXp Chamber	22
3.2.2 St-1 D0VVp Chamber	23
3.2.3 St-2 D2UUp Chamber	26
3.3 Gas Flow System	29
IV. DRIFT CHAMBERS STUDIES	35

4.1	Chamber Efficiency	35
4.1.1	Statistical Uncertainty Calculation	36
4.2	Extraction of Calibration Parameters	37
V.	SUMMARY AND OUTLOOK	51
	REFERENCES	53

LIST OF TABLES

Table 3.1	Debugging and resolution of D0XXp wire's channels	21
Table 3.2	Debugging and resolution of D0UUp wire's channels	22
Table 3.3	Debugging and resolution of D0VVp wire's channels	22
Table 3.4	Running and flushing flow rates for various drift chambers	33
Table 4.1	In-plane efficiencies and their uncertainties for St-2 and St-3 DC extracted for a cosmic ray run # 2155 taken on November 2020. The evaluation was done with 10176 tracklets, out of which 3094 have a number of hits higher than 11 and 2711 have $RdChisq < 1$	37
Table 4.2	Station IDs for each drift chamber	40

LIST OF FIGURES

Figure 1.1	Drell-Yan Process.....	1
Figure 1.2	PDFs x_B dependence	3
Figure 1.3	Quark annihilation and gluon fusion cross sections ratio as a function of x_F for cc production in p-p collisions [3], plotted at SpinQuest $E_{cm} = 15$ GeV.....	3
Figure 1.4	AN anticipated uncertainties for J/ψ production and one week of data-taking at SpinQuest.....	5
Figure 2.1	E1039/SpinQuest spectrometer	7
Figure 2.2	Schematic of the E1039/SpinQuest spectrometer in the xz deflection plane	8
Figure 2.3	The iron focusing magnet, FMAG	10
Figure 2.4	The KTeV momentum-measuring magnet, KMAG.....	10
Figure 2.5	Hodoscope planes at the first (a) and fourth (b) stations.....	11
Figure 2.6	An illustration of the electrons ionization avalanche [10].....	12
Figure 2.7	Positive (left) and negative (right) HV power supplies used for various drift chambers.....	13
Figure 2.8	NM4 control room.....	14
Figure 3.1	A schematic of the DC electronic readout chain before/after swapping the ribbon cables connecting LSBs and ASDQs (left/right).	18
Figure 3.2	D0U (left) and D0Up (right) hit distributions for a cosmic run 2925 taken with a HV set at 1.45 kV where the inefficient wires, 149-153, are apparent.	20
Figure 3.3	D0U (left) and D0Up (right) hit distributions for a cosmic run 3745 taken with a HV set at 1.55 kV, where the problem of inefficient D0Up wires, 149-155, is resolved. While D0Up dead wire # 113 has recovered after fixing its ASDQ card connectivity.....	20

Figure 3.4	An illustration of D0X repair after attaching two new (blue) capacitors to the HV bus.....	23
Figure 3.5	D0VVp chamber after moving it to the NM4 loading dock, where it's lying flat instead of its vertical position in the spectrometer.....	24
Figure 3.6	Adopted test setup for checking capacitors with HV ON	25
Figure 3.7	Charging and discharging signal of a capacitor measured by the oscilloscope	25
Figure 3.8	HV test circuit where the top circled part of an additional resistor and oscilloscope is added to the typical chamber's components to check various capacitors.....	26
Figure 3.9	D2U sense plane after removing the top cathode plane	27
Figure 3.10	Covered resistors with Kapton tape.....	27
Figure 3.11	Gas flow chart from the external gas shed (left side) up to experimental hall flow meters racks (right side).....	29
Figure 3.12	Some St-1 DC planes dimensions	30
Figure 3.13	Some St-2 DC plane's dimensions.....	30
Figure 3.14	Some St-3 top-half DC plane's dimensions.....	31
Figure 3.15	Some St-3 bottom-half DC plane's dimensions.....	31
Figure 4.1	The sketch of the xz extraction at $z= 1900$ cm corresponding to u plane of D3m chamber	38
Figure 4.2	The sketch of the yz extraction at $z= 1900$ cm corresponding to u plane of D3m chamber	39
Figure 4.3	Drift distance distribution.....	40
Figure 4.4	Track distance distribution	41
Figure 4.5	Drift distance, R , as a function of track distance, D	41
Figure 4.6	Residual and TDC time, t , correlation.....	41
Figure 4.7	Illustration of the extracted RT curve in terms of the drift distance, R , and the TDC time, t (ns) correlation	42
Figure 4.8	Drift time, T , as a function of signed drift distance, R	42

Figure 4.9	tx distribution for D3mU plane with the allowable range shown with dashed red lines	43
Figure 4.10	ty distribution for D3mU plane with the allowable range shown with dashed red lines	44
Figure 4.11	The x-position distribution at $z= 1900$ cm, corresponding to D3mU plane with the allowable range shown with dashed red lines	44
Figure 4.12	The y-position distribution at $z= 1900$ cm, corresponding to D3mU plane with the allowable range shown with dashed red lines	45
Figure 4.13	tx distribution for D2X plane with the allowable range shown with dashed red lines	46
Figure 4.14	ty distribution for D2X plane with the allowable range shown with dashed red lines	47
Figure 4.15	x_0 distribution for D2X plane with the allowable range shown with dashed red lines	47
Figure 4.16	y_0 distribution for D2X plane with the allowable range shown with dashed red lines	48
Figure 4.17	The x-position distribution at $z= 1347$ cm, corresponding to D2X plane with the allowable range shown with dashed red lines	48
Figure 4.18	The y-position distribution at $z= 1347$ cm, corresponding to D2X plane with the allowable range shown with dashed red lines	49

LIST OF SYMBOLS, ABBREVIATIONS, AND NOMENCLATURE

DY	Drell-Yan
QCD	Quantum Chromodynamics
TSSA	Transverse Single Spin Asymmetries
CM	Center of Mass
FMAG	Focusing Magnet
KMAG	KTeV Momentum-measuring Magnet
RF	Radio Frequency
ASDQ	Amplifier-Shaper-Discriminator-Charge Integrator
LSB	Level Shifter Board
TDC	Time to Digital Converter
DC	Drift Chamber
LEMO	Léon Mouttet - Electronic and fibre optic connector
HV	High Voltage
PS	Power Supply
ASDQ	Amplifier-Shaper-Discriminator-Charge Integrator (Q)
FPGA	Field-Programmable Gate Array
QIE	Charge Integrator and Encoder
RFQ	Radio-Frequency Quadrupole
PMT	Photo Multiplier Tube

DAQ Data Acquisition System

CHAPTER I
INTRODUCTION

1.1 SpinQuest Motivation

The Fermilab E1039/SpinQuest experiment aims to measure the quark structure of protons and neutrons, mainly the sea-quark Sivers function [1]. The experiment involves colliding an unpolarized 120 GeV proton beam with transversely polarized cryogenic targets, NH_3 (as a proton target) and ND_3 (as a neutron target) in order to measure the process $q + \bar{q} \rightarrow \gamma^* \rightarrow \mu^+ \mu^-$, the so-called Drell-Yan process, see Fig. 1.1.

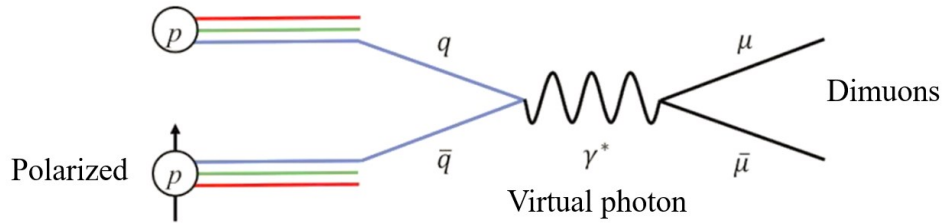


Figure 1.1 Drell-Yan Process

In these collisions, a quark from the proton beam annihilates with an anti-quark from the polarized target and forms a virtual photon, which subsequently decays into a di-muon ($\mu^+ \mu^-$) pair. The experiment will allow the extraction of spin dependent quark and anti-quark distributions of the proton and neutron and study the unique behavior of a correlation between the quark/anti-

quark spin and angular momenta. The angular distributions of the polarized DY process can also be used to test higher order corrections to the QCD description of the DY scattering cross sections.

1.2 First-publication Physics Goals

The SpinQuest experiment also provides a unique opportunity to study the poorly known gluon Sivers/Twist-3 correlation functions using J/ψ production at a very interesting kinematic phase space coverage. Large transverse single spin asymmetries (TSSAs) up to $\cong 40\%$ have been observed in light hadron production, such as J/ψ , in the forward region of the Feynman scaling variable x_F , corresponding to the mid. region of proton momentum fraction x_B [2]. Although these effects have been largely attributed to the valence sector, Fig. 1.2 manifests the potential of a substantial gluons contribution given their primary population of x_B below 0.22. As depicted in Fig. 1.3, at SpinQuest's center-of-mass (CM) energy of 15 GeV and our x_F range from 0.3 to 0.8, the gluon-gluon fusion begins to dominate as the primary mechanism for J/ψ production. Therefore, the proposed study will allow investigating the observed TSSAs in J/ψ production and gluon Sivers functions.

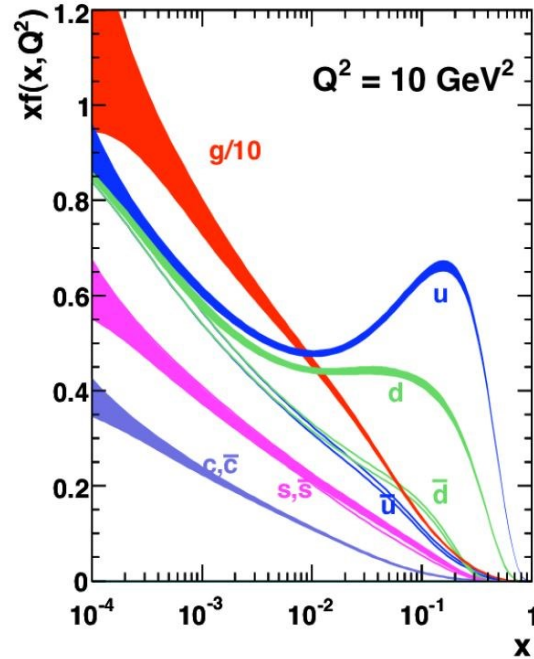


Figure 1.2 PDFs x_B dependence

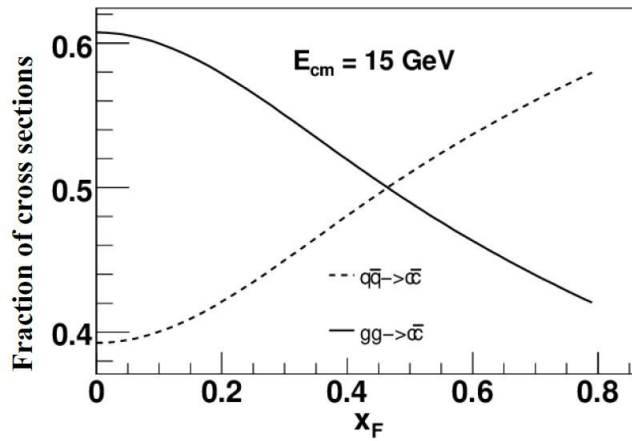


Figure 1.3 Quark annihilation and gluon fusion cross sections ratio as a function of x_F for $c\bar{c}$ production in p-p collisions [3], plotted at SpinQuest $E_{cm} = 15$ GeV.

Based on the ongoing simulation studies, we expect having good statistics from one week of dedicated data-taking on J/ψ production to measure this asymmetry with a good precision.

Figure 1.4 illustrates the anticipated uncertainty for this asymmetry, A_N , measurement, which is defined as

$$A_N = \frac{2 \sum_i N(x_T, \phi_{S_i}) \sin \phi_{S_i}}{f \sum_i N(x_T, \phi_{S_i})} \quad (1.1)$$

where N is the dimuon yield at a given x_B target (x_T) and azimuthal angle ϕ_{S_i} , the target's transverse spin orientation. A_N is extracted from the simulation of reconstructed charmonium production by taking into account the SpinQuest dimuon acceptance, which is scaled by the expected one week experimental data integrated luminosity, $L_{1\omega}$, of $7e4 \text{ pb}^{-1}$, the simulation integrated luminosity, L_{sim} , of 8414.86 pb^{-1} , the polarized target's Nitrogen dilution factor, f , of 0.176, and the expected target polarization, P , of 80 %. However, the anticipated uncertainty is evaluated as follows,

$$\delta_{A_N}^{1\omega} = \frac{\delta_{A_N}^{sim}}{fP} \sqrt{\frac{L^{sim}}{L^{1\omega}}} \quad \text{where} \quad \delta_{A_N}^{sim} \sim \frac{1}{\sqrt{N_{measured}}} \quad (1.2)$$

Given the good statistical precision expected for these x_T bins and the exciting physics potential, this measurement is part of our “Day-one” physics program and its analysis is prioritized as the first SpinQuest publication.

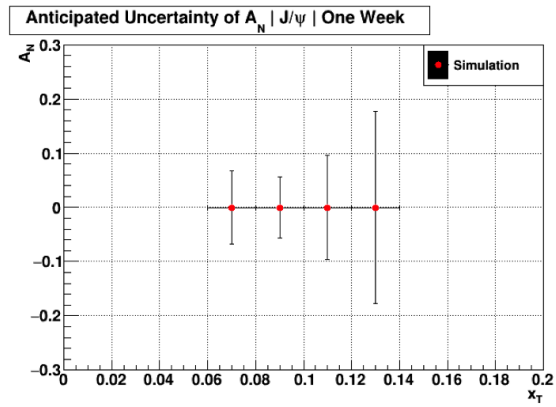


Figure 1.4 A_N anticipated uncertainties for J/ψ production and one week of data-taking at SpinQuest

(Courtesy of our group's postdoc Dr. C. Ayuso)

CHAPTER II

EXPERIMENTAL SETUP

The inherited SpinQuest spectrometer from the predecessor DY experiments, including the latest SeaQuest experiment [4,5], is supplied in this project with a target system consisting of a 5 T superconducting magnet, transversely polarized NH_3 and ND_3 targets, a ^4He evaporation refrigerator, a 140 GHz microwave source, and a large pumping system. [6] The spectrometer is based on a focusing magnet (FMAG), which plays a role of a beam dump and first hadron absorber, three stations (St) of drift chambers (DC), four stations of hodoscopes, a momentum-measuring magnet (KMAG), and a second hadron absorber preceding the last tracking station of proportional tubes, see Fig. 2.1 where the proton beam travels from left to right. This spectrometer is designed to select oppositely charged muon pairs at 4-9 GeV mass range, and to assure the pairs detection based on its four stations of trackers and hodoscope scintillators as well as the last hadron absorber.

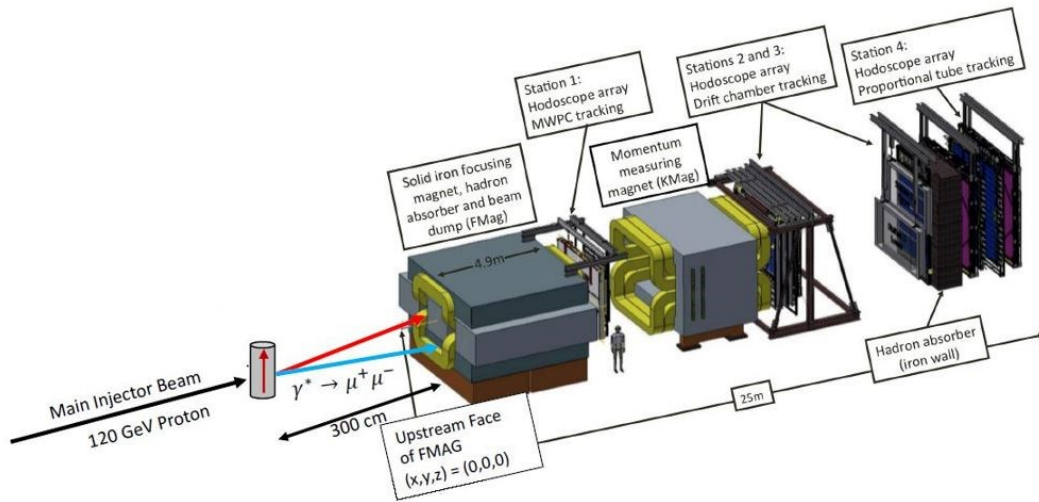


Figure 2.1 E1039/SpinQuest spectrometer

In the spectrometer's lab. frame convention, the direction of the proton beam is considered as the z direction. The y -axis is defined vertically upward, while the x -axis is determined according to the right-hand rule using the z - and y -axes directions. The frame origin, $z = 0$ cm, corresponds to the upstream edge of the first magnet, FMAG. [6] The schematic diagram illustrated in Fig. 2.2 shows the locations of the spectrometer's components in xz plane.

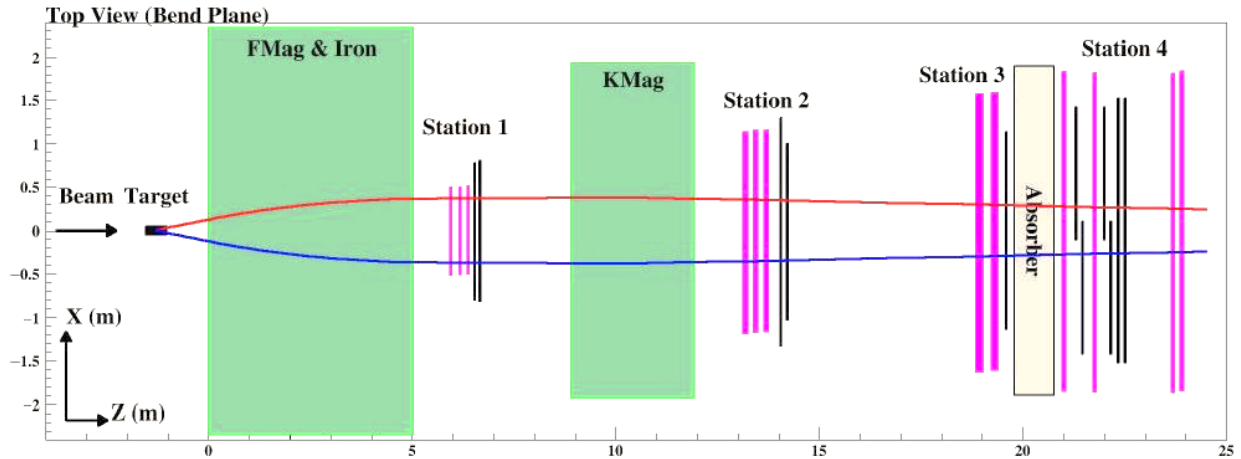


Figure 2.2 Schematic of the E1039/SpinQuest spectrometer in the xz deflection plane

2.2 Beam

The beam is initially produced by accelerating ionized hydrogen in a static electric field up to 35 keV. Then, the stream of protons is passed into a Radio-Frequency Quadrupole (RFQ) with a frequency of 53.1 MHz, which get accelerated up to 750 keV. The RFQ splits the beam into 2 ns buckets, which are 18.8 ns apart. The beam is then sent into a linear series of superconducting RF cavities which accelerate the protons and send them to the Booster. The full circumference of the Booster holds 84 buckets. The group of buckets is transferred then to the Main Injector, which accelerates the protons up to the required 120 GeV beam energy. The target receives the beam over five seconds through slow-spill extraction method because of its high intensity of about 10^4 protons per bucket. Each of these five seconds spill are followed by a fifty-five seconds gap as the Main Injector recharges and sends beam to other experiments. This in-between spills gap gives the opportunity for the DAQ system to recover and helps lowering the radiation in the target cave. [7]

2.3 Target

SpinQuest intends to use a polarized NH_3/ND_3 target system with a high-cooling-power evaporation refrigerator connected to a large pump stack ($14,000 \text{ m}^3/\text{hour}$) and a microwave generator for a dynamic polarization of the target nucleons. The polarization magnet possesses a 5 T field with a homogeneous 8 cm region to ensure the polarization of all nucleons, protons and neutrons, in each target. [8,9]

2.4 Magnets

The first solid iron magnet, FMAG, is primarily used as a combination of a hadron absorber, bending magnet, and beam dump, see Fig. 2.3. This magnet absorbs the enormous number of charged hadrons (primarily pions and kaons) produced in the target and performs the first bending of the muons that the SpinQuest seeks to detect. The second magnet in the spectrometer is KMAG, which is the momentum measuring magnet, and unlike the FMag it has an open aperture, see Fig. 2.4. [6] During the last E906/SeaQuest experiment, KMAG was run at 1600 A (270 V using 430 kW of power) to generate a magnetic field of 0.4T (giving a total magnetic deflection of about 0.39 GeV/c). The field of both KMAG and FMAG magnets was oriented vertically along the $+y/-y$ direction in the first/last part of the E906 experiment, the convention that might be used in the E1039 experiment as well. This change is typically performed to identify any left-right asymmetries present in the spectrometer. The vertical orientation of the magnetic field is thus defining the deflection plane which is, in this case, along the x-direction.

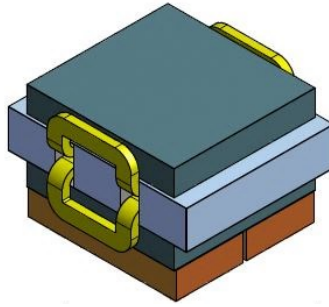


Figure 2.3 The iron focusing magnet, FMAG

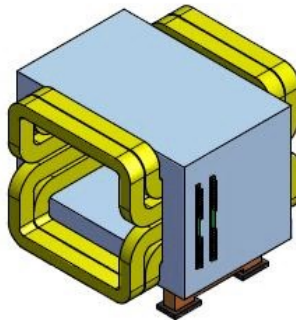


Figure 2.4 The KTeV momentum-measuring magnet, KMAG

2.5 Hodoscopes

SpinQuest uses scintillator hodoscope planes at four stations of its spectrometer. They are named as x-measuring hodoscopes (HNX) and y-measuring hodoscopes (HNY), with respect to the paddles orientation. Each plane is split into two parts at the first (see Fig. 2.5 left) and second hodoscope's stations. The x-measuring hodoscopes are split into top (e.g., H1XT) and bottom (e.g., H1XB) halves. The y-measuring hodoscopes are split left and right, e.g. H2YL and H2YR. A single plane of x-measuring hodoscopes exists at St-3 (noted as H3X) and St-4 (noted as H4X), while two planes of y-measuring hodoscopes (H4Y1 and H4Y2) is located at St-4, see Fig. 2.5 right.

LeCroy 1440 high voltage system provides HV for all hodoscope's PMTs, and this process is controlled using the internal network. Each 1443 card has 16 independently controlled HV outputs. The hodoscope working-group is performing studies to set the nominal HV for the four E1039 spectrometer stations, but the latter was set at 1400 to 2000 Volts in the previous E906 experiment.

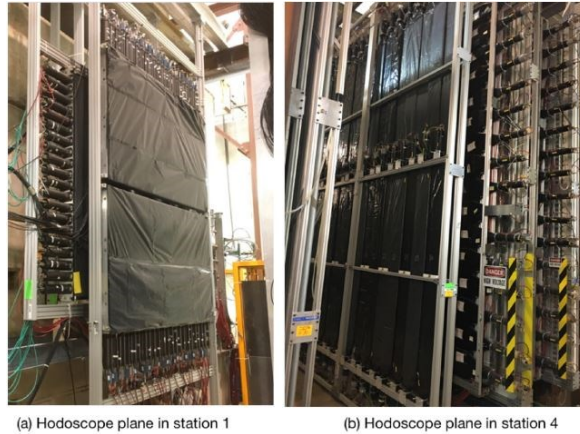


Figure 2.5 Hodoscope planes at the first (a) and fourth (b) stations

2.6 Drift Chambers

All drift chambers have the same basic structure. Each of these chambers consists of a sandwich of two sense planes and top and bottom cathode planes. On x and x' planes, wires are aligned in the vertical direction while wires are tilted by $\pm 14^\circ$ on the other $(u, u')/ (v, v')$ planes. On the primed planes, wires are offset by a half drift cell to resolve the left-right ambiguity of drift direction. All DC planes are mounted in the spectrometer perpendicular to the z axis, and each drift cell is rectangularly shaped. The nomenclature used for the three DC stations is as follows: D0 for St-1, D2 for St-2, and D3p/D3m for St-3 top/bottom half. Furthermore, the employed

notation for their planes is composed of the defined chamber's name followed by the plane type, e.g., D0X, D0U and D0V for the unprimed x, u and v planes, and D0Xp, D0Up and D0Vp for the primed x', u' and v' planes.

Given the basic operational principle of DCs is similar to any gaseous detector, in which the passage of charged particles stimulates its gas atoms ionization, DCs are exploited in SpinQuest to detect mainly the oppositely charged muons. Due to the mentioned in-medium ionization, a number of electron-ion pairs are created leading to a cascade of primary and secondary electrons, namely an avalanche, as depicted in Fig. 2.6, which drifts toward the positively charged anode (sense) wire while the produced ions merge towards the cathode thus a signal at the electrodes is generated. As a result, the measurement of electrons' drift time provided by TDCs gives an estimation of the drift distance of reconstructed tracks from the sense wires, the known as RT curve which is described in Ch. 4.

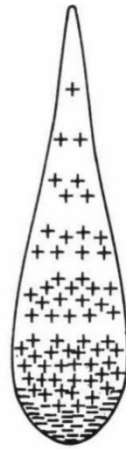


Figure 2.6 An illustration of the electrons ionization avalanche [10].

During the cosmic ray commissioning, drift chambers are operating with ArCO₂ gas mixture while their HV is supplied by a positive (for St-1 D0 chambers) and negative (for St-2 D2

and St-3 D3p/m chambers) HV Power Supplies (see Fig. 2.7) located at NM4 control room racks (see Fig. 2.8) from which they are connected with long HV cables to all chambers mounted underground in the experimental hall. At this point, the nominal HV for different chambers is set roughly at 1.55 kV for St-1 D0, 1.90 kV for St-2 D2, and 2.48 kV for St-3 D3p/m chambers. These values are expected to change close to the beam commissioning once the gas is changed to the production gas mixture, P8CF4.



Figure 2.7 Positive (left) and negative (right) HV power supplies used for various drift chambers



Figure 2.8 NM4 control room

2.7 Proportional Tubes

The last tracking station is composed of four planes of proportional tubes, which are mainly used for clean muon identification. The latter is possible due to the iron wall, which is defined in Fig. 2.1 as the second hadron absorber, and is located in between station 3 and station 4 (St-4). Each of these planes contain 8 tubes of 5.08 cm diameter and $\cong 0.15875$ cm thickness. The tubes operates with ArCO₂ gas mixture, and their operational mode is similar to drift chambers. [8].

2.8 Trigger

The main experiment trigger is the FPGA trigger, which is comprised of several levels of logic gates. All levels use CAEN v1495 6U VMEbus modules, which are named as v1945s. [9] Each module has a TDC, which stores the time information as it reads the signals from the hodoscope paddles.

2.9 Data Acquisition

The DAQ systems are anticipated to remain as in the previous SeaQuest experiment in which they were divided into four parts. The Main DAQ is primarily used for processing and reading out

various detector's signals in event-by-event basis. The Beam DAQ controls the outputs from the QIE. The counters readouts are handled by the Scalar DAQ in a spill-by-spill basis. [9]

CHAPTER III

DRIFT CHAMBER REPAIR AND DEBUGGING

The drift chambers mounted in E1039 spectrometer initially suffered from some HV or readout components problems which needed to be debugged. For example, some DC hit distributions were showing some deficient, dead, or noisy regions as an indication of problems with either the associated sense wires' planes or electronic components in the readout chain, thus a thorough investigations were needed to debug and thus resolve the issue. While some other chambers were having frequent HV trips or even a dead short thus they were unmounted from the spectrometer for inspection and repair.

3.1 Problematic Hit Distributions Channels

The investigation work that has been done to debug inefficient/noisy/dead channels mainly in St-1 and St-2 DC is summarized in this section. The objective of this work was to determine whether the problem is internal or external and thus can be fixed by simply replacing some electronic readouts. In case of the former and depending on the repair complexity, a decision had to be made by the DC group to either pull the chamber out for restoration or leave it as is particularly if the few impaired channels in the plane won't affect its performance or efficiency. During the debugging process, either the internal structure or the following elements of the external readout chains had to be checked:

- 1) TDC boards
- 2) Ribbon cables connecting TDCs and LSBs
- 3) Level Shifter Boards
- 4) Ribbon cables connecting LSBs and ASDQ cards
- 5) ASDQ cards
- 6) ASDQ cards pins on each chamber's plane

The detailed debugging for each itemized step is as follows

- 1) TDCs - this is the less probable cause and easy to fix. TDCs can be power-cycled to see if it makes a difference. When swapping two ribbon cables, if the problematic channel is not shifted in the new hit distributions, then the problem should be coming from the TDC side. Also, the LEMO cable on TDC can be checked because a malfunctioning cable can cause a region of dead channels in the hit distributions. For example, the E1039 cosmic ray run # 2558 had dead region which was caused by a bad LEMO cable on D0UUp chamber thus replacing it fixed the problem.
- 2) Swapping the ribbon cable connecting TDCs and the front side of LSBs can be done in the TDCs or LSBs side. If the former shifts the symptom in the hit distributions and the latter don't, then the ribbon cable is bad and thus replaced. This conclusion is of course made after double-checking that the related TDC board is working fine.
- 3) LSBs – If they are the suspect, one can start by power-cycling their crate or issuing a "reset" command from any internal server nodes. [11] If that doesn't resolve the problematic channel(s) issue and if they are also oscillating/noisy, increasing the LSB threshold could help

but that should be performed with cautious as very high thresholds can lower the DC plane(s) efficiency.

The bad LSB fuses could also cause uneven behavior in the hit distributions. Their warnings can be checked on the board's LEDs or remotely at any internal node [11]. If the two LEDs are ON on the board, that means at least one fuse could be bad. In such a case, the board is removed to test and replace fuses. In addition, swapping the ribbon cables in the back-side of LSBs is typically employed to check the LSB health as the latter will be bad and needs to be replaced/fixed if the symptom won't move with the traded cable.

- 4) After performing above checks, if the readout channels are good up to LSBs then the ribbon cables connecting LSBs and ASDQ cards should be tested on the chamber side. As a result, if swapping ribbon cables between two ASDQs (see Fig. 3.1) would shift the symptom in the hit distributions, then the cable is bad and must be replaced.

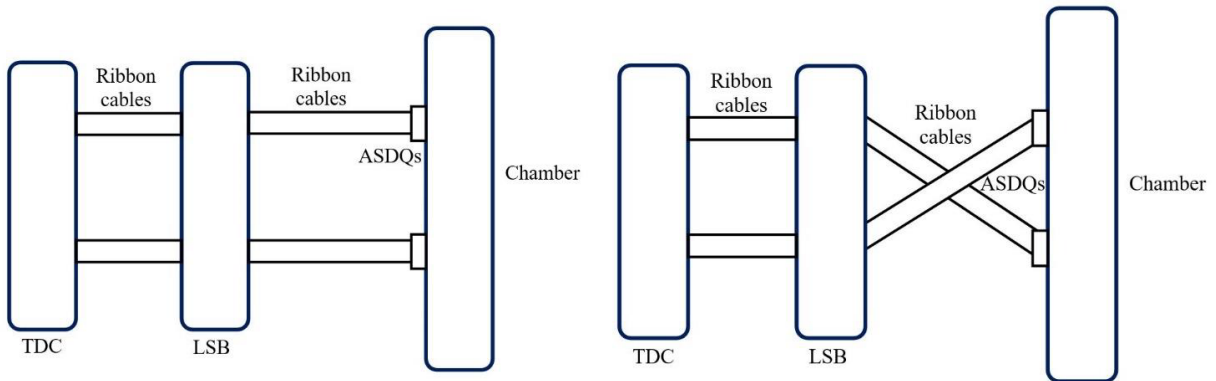


Figure 3.1 A schematic of the DC electronic readout chain before/after swapping the ribbon cables connecting LSBs and ASDQs (left/right).

- 5) In case the last steps will prove that all downstream electronic chain components are good, then ASDQ cards will be swapped to test them. If the problematic region is not shifted in the new hit distributions, then the card is deficient and must be replaced.
- 6) If the ASDQ is also good, then the last external check is related to the ASDQ card pins on the corresponding chamber's plane. For example, some bended pins were found on the D2U plane, which of course was not possible to fix them as observed. Given the chamber had to be unmounted from the spectrometer to be repaired for a different reason, then those pins were fixed too. A nonconductive adhesive was utilized to seal the ASDQ pin holder.

In case the execution of the described external debugging steps won't fix all inefficiency/dead channels issue, the problem is related then to the internal structure of that chamber's plane(s). One remedy could be increasing the HV to improve the efficiency of these channels. For example, D0Up plane was suffering from some inefficient channels in element IDs 149-153 as in cosmic ray run 2925, see Fig. 3.2, where the HV was set at 1.45 kV. However, increasing the HV to 1.55 kV had solved these channels inefficiency as depicted in Fig. 3.3. The figure also illustrates the effect of debugging the external readout chain by fixing the D0Up element ID 113, while D0U element ID 101 was left as is given it's a dead wire which can't be repaired due to the issue of the double-sticky tape used as a gas seal for these more than 30 years old chambers.

Run 2925, Spill 1-2074 (N=2064), Event 7081132 (N=650104)
Drawn at 2021-06-04 12:12:07

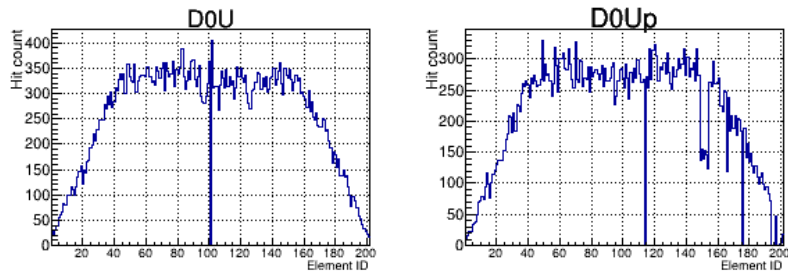


Figure 3.2 D0U (left) and D0Up (right) hit distributions for a cosmic run 2925 taken with a HV set at 1.45 kV where the inefficient wires, 149-153, are apparent.

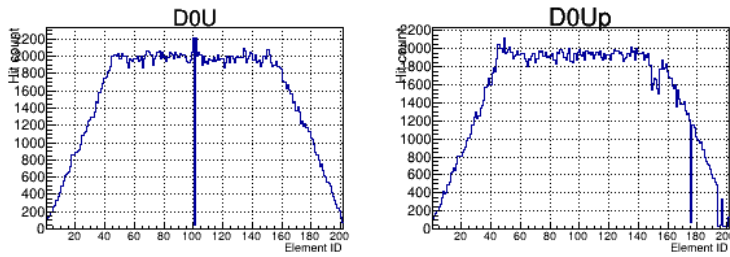


Figure 3.3 D0U (left) and D0Up (right) hit distributions for a cosmic run 3745 taken with a HV set at 1.55 kV, where the problem of inefficient D0Up wires, 149-155, is resolved. While D0Up dead wire # 113 has recovered after fixing its ASDQ card connectivity.

Tables 3.1, 3.2, and 3.3 contain an up-to-date summary of the mentioned debugging and resolution work for St-1 DC planes as a preparation for the upcoming fall commissioning period with proton beam.

Table 3.1 Debugging and resolution of D0XXp wire's channels

	Bad wire #	Run#	Dead/Inefficient /Noisy	Conclusion/Comment	Status	OK from which run
D0X	33-94		Noisy	LSB issue	Resolved	3606
	70-73		Noisy	Internal	Leave	
	73	3600	Inefficient	Blown fuse on LSB (board 1)	Resolved	3606
	85	3601	noisy	Blown fuse on LSB (board 1)	Resolved	3606
	65-96	3600	almost dead	Blown fuse on LSB (board 1)	Resolved	3606
	92-94	3600	Inefficient	Blown fuse on LSB (board 1)	Resolved	3606
	95	3600	noisy	Blown fuse on LSB (board 1)	Resolved	3606
	40	3612	Dead	Cable connection on TDC	Resolved	3618
	56	3613	Dead	Cable connection on TDC	Resolved	3618
	59, 60, 61, 63	3620	Almost dead	These channels were shifted in the hit distributions by correcting TDC cable connection and LSB front cabling, location kept by swapping cables at LSB backside. This was related to a LSB issue. Replaced LSB and it was gone, but ID=6,7 got inefficient (run3641). Replaced LSB back with a new one. In run 3648, 60 and 61 channels seems inefficient. Replaced LSB again, and in run 3651, 60 61 channels seems still inefficient. Therefore swap ribbon cables from front LSB	Resolved	3641 (59,63)
	60,61		Inefficient	Newly appeared in run3648. LSB was not the problem. Swap ASDQ on the chamber and check if it's coming from inside the chamber.	Leave	
	84, 86, 87	3615	Inefficient	Cable (from ASDQ to LSB) issue. 84 and 86 are inefficient. Replaced cable and resolved? ID=84 seems still inefficient in run 3648. When swapping ASDQ, the channel was shifted in run 3651. Therefore ID=84 is coming from inside the chamber, and leave this channel.	Leave (Element ID=84)	
	104	3614	Dead	Cable connection on LSB	Resolved	3618
	113-128	3614	noisy	Cable connection on LSB	Resolved	3618
	120	3614	Inefficient	Cable connection on LSB	Resolved	3618
	160	3612	Inefficient	Internal	Leave	
	155-157	3612	Inefficient	Only 155 is inefficient. Internal	Leave	
	145, 146	3612	Dead	Internal	Leave	
D0Xp	12, 13	3594	Inefficient	Internal	Leave	

Table 3.2 Debugging and resolution of D0UUp wire's channels

	Bad wire #	Run#	Dead/Inefficient /Noisy	Conclusion/Comment	Status	OK from which run
D0U	101		Dead	Internal	Leave	
D0Up	113	2802	Dead	ASDQ connectivity has been causing the noise. Run 3641 has no noisy channels in this region.	Resolved	3646
	166	1573	Inefficient	This inefficient channel has been gone since run 3612 by increasing	Resolved	3612
	176	2490	Inefficient		Leave	
	106-108	3620	noisy	Newly appeared (Run 3611) The noisy pattern looks different in run3619, after correcting the bad connection on TDC. ASDQ connectivity has been causing the noise. Run 3641 has no noisy channels in this region.	Resolved	3646
	194-201	1305	Inefficient	Internal	Leave	
	149-155	1305	Inefficient	Internal, happens when HV is low	Leave	

Table 3.3 Debugging and resolution of D0VVp wire's channels

	Bad wire #	Run#	Dead/Inefficient /Noisy	Conclusion/Comment	Status	OK from which run
D0V	86	From e906 time (#028700)	Inefficient	Internal	Leave	
	65-96	3571	Dead	Cable on TDC, resolved	Resolved	
	170-201	2970	Dead	Cable on TDC, resolved	Resolved	
	170-185		Inefficient	Upside down cable on LSB, resolved	Resolved	
D0Vp	71-72	2970	Dead	Gone, seems cable connection at TDC side (Run 3612)	Resolved	3612
	88	3565	Inefficient	LSB had problem, resolved	Resolved	
	101	From E906 time (#028700)	Dead	Internal	Resolved	3615
	138	3565	Dead	LSB had problem, resolved	Resolved	
	139-145	3612	Dead	Cable connection on LSB.	Resolved	3618
	146	From E906 time (#028700)	Inefficient	Internal	Resolved	
	178-179	From E906 time (#028700)	Inefficient	Internal	Leave	
	186-187	From E906 time (#028700)	Inefficient	Internal	Leave	

3.2 Drift Chambers Repair

3.2.1 St-1 D0XXp Chamber

In this first station, the D0X plane of D0XXp chamber had suffered from a HV dead-short which required pulling out the chamber and moving it to another Fermilab lab, known as Lab6, to debug and thus resolve the problem. This investigation has started by testing the series of resistors and capacitors connected to the sense wires electronic traces inside the chamber. Using a voltmeter,

it was found that the reading of two resistors and capacitors pairs was out of range (or Over Load) as measured by the device. To complete this test, these two 10 nF capacitors were disconnected and thus the plane started holding HV at the nominal value of 1.55 kV. Given the plane was running stable on HV for a couple of days, new capacitors were ordered and soldered to the HV bus, see Fig. 3.4 where blue capacitors represent the newly connected capacitors. After a stable operation of D0XXp once this fix was applied, the chamber was moved back to NM4 and mounted in the spectrometer.



Figure 3.4 An illustration of D0X repair after attaching two new (blue) capacitors to the HV bus.

3.2.2 St-1 D0VVp Chamber

Once again in this station, the D0Vp plane of D0VVp chamber start suffering from frequent HV trips whenever the HV is set at a value higher than 1.0 kV. To determine which side of D0Vp plane is causing this HV instability, HV was applied to the top side at which the plane was running stable up to HV of 1.55 kV. However, once the HV was applied only to the bottom side, it started tripping around a value of 1.3 kV as an indication that this HV problem is originating for this side of the plane. Based on the described experience with D0XXp chamber, the pair of resistors and

capacitors in this bottom side had to be tested thus the chamber had to be unmounted and moved to the NM4 loading dock, as shown in Fig. 3.5. Given the simple test method used for D0X plane based on a voltmeter measurement to identify any bad resistor or capacitor didn't show any deficient component, a new test method has to be developed for this kind of test but while applying HV.

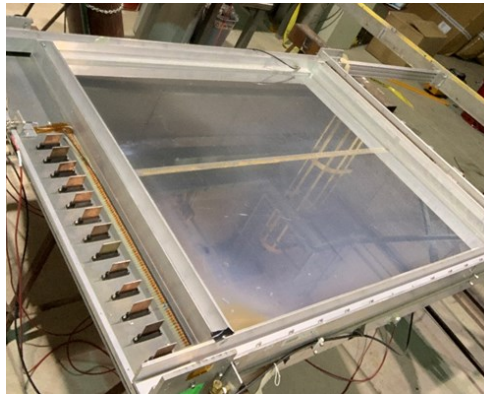


Figure 3.5 D0VVp chamber after moving it to the NM4 loading dock, where it's lying flat instead of its vertical position in the spectrometer

Figure 3.6 illustrate the test setup that was adopted for checking capacitors with HV ON. Qualitatively, no difference was observed in the time it takes to overload the voltmeter while checking different capacitors. As a result, a quantitative measurement had to be performed of the charging and discharging time constant using a 1200 Hz (approx. 4.91 V) signal generator and an oscilloscope. The observed signal of the RC circuit consisting of a 5.7 M Ω resistor and a 10 nF capacitor leading to a τ of 0.6 ms, is depicted in Fig. 3.7.

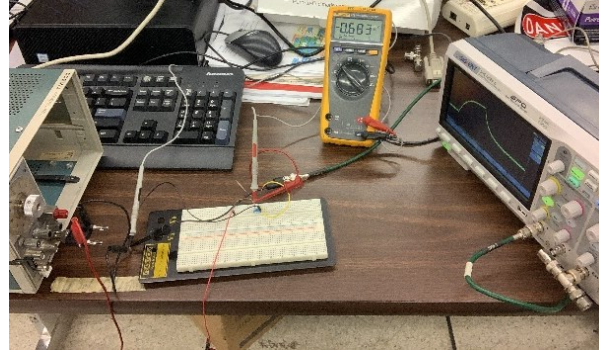


Figure 3.6 Adopted test setup for checking capacitors with HV ON

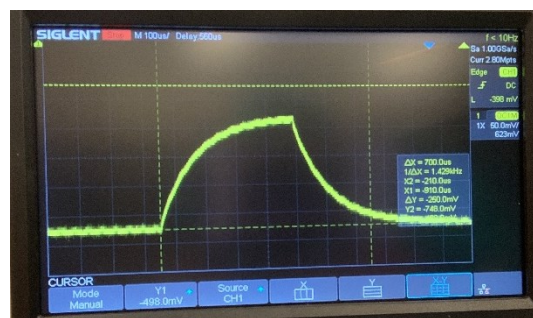


Figure 3.7 Charging and discharging signal of a capacitor measured by the oscilloscope

Figure 3.8 illustrates all components of the adopted circuit to test the D0Vp capacitors while applying HV. The provided leak current by the attached oscilloscope to the typical chamber's HV circuit elements is expected to be high for bad capacitors compared to good ones. However, these test results were identical for all capacitors indicating that they are all good.

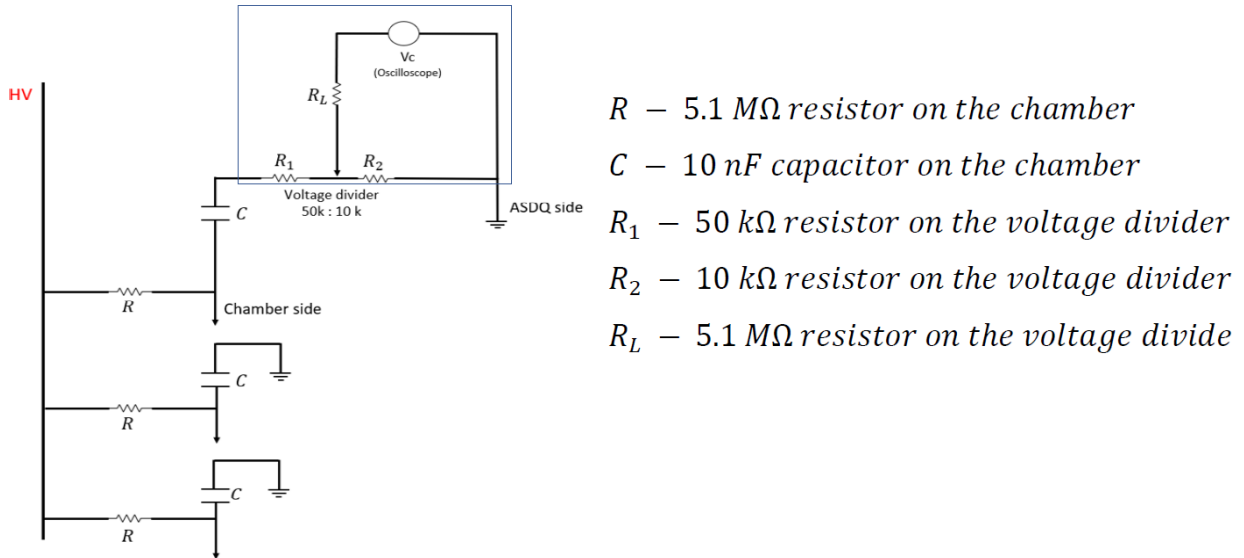


Figure 3.8 HV test circuit where the top circled part of an additional resistor and oscilloscope is added to the typical chamber's components to check various capacitors.

At this point, most known debugging methods were exhausted without resolving the mysterious HV trips, thus we had to flip the chamber back to the nominal vertical orientation, apply HV, and watch the leak current behavior. Surprisingly enough, after gradually increasing HV and keeping the leak current at 1 μ A scale, the plane was holding HV in both top and both sides for an extended period of time of a week or so. By the end, we have concluded that the HV trip could somehow be related to some "dust" or "irregular fragments" that changing the chamber's orientation helped get rid of their charging effect. Based on that, the chamber was mounted back on the spectrometer where it's currently running stable with HV.

3.2.3 St-2 D2UUp Chamber

While the D2UUp chamber was mounted in the spectrometer, the D2U plane was having frequent HV trips until the level it was not holding HV anymore due to the high leak current. At

this point, the chamber was moved to Lab6 for investigations. Figure 3.9 shows the D2U sense plane after opening it. By applying HV solely to this sense plane, an ohmic behavior was observed given the voltage tripped at a value of 0.1 kV where the leak current at 10 μA scale, corresponding to a resistance of about 12.5 M Ω . In this process, some electric sparks were heard/seen in between the sense plane and the G10 spacer. After removing the spacer, all resistors including their soldered edges were covered with a Kapton tape, see Fig. 3.10, and that was enough to resolve both the sparks as well as the HV trips issues. Furthermore, the plane was cleaned with a nitrogen gun to remove any dust fragments and thus closed for a longer HV test. The chamber was supplied temporarily with N₂ gas to perform its HV training, which end up being a success since this chamber's side started holding HV up to its nominal value of 1.95 kV with a very low leak current in the range of 0.02 μA .



Figure 3.9 D2U sense plane after removing the top cathode plane



Figure 3.10 Covered resistors with Kapton tape

While the D2Up was holding HV when the chamber was mounted at NM4, it was observed upon the chamber's arrival at Lab6 that its inner cathode plane is not holding HV with a similar ohmic behavior of D2U sense plane. Upon fixing the unprimed side issue, the chamber was flipped to investigate the D2Up cathode plane problem. Inspecting the latter was somehow tedious with some bizarre behavior as the plane seems holding HV when all top components (outer cathode + G10 spacer + sense plane) are removed, and not otherwise. Given electric sparks were heard/seen in this side as well, all resistors in the D2Up sense plane was covered with a Kapton tape to solve this additional issue that, of course, had nothing to do with the inner plane behavior.

After a detailed inspection of all electric circuits components as well as their connection, it has been observed that electrical connection of the mylar plane underneath the inner cathode plane is broken. This mylar plane is composed of three sheets vertically aligned and connected with a copper tape that had worn off in some places. This issue was fixed by applying a conductive adhesive to restore the electrical connection between the affected mylar sheet's areas. By doing so, the HV trip of D2Up inner cathode plane was resolved, and thus the chamber was cleaned with nitrogen and assembled back for a HV training. Similarly to D2U, the chamber was supplied temporarily with N₂ gas during the HV training, which was also successful as D2Up was able to hold HV up to its nominal value of 1.95 kV with a very low leak current in the range of 0.02 μ A. By the end of this test, the D2UUp chamber was moved back to NM4 and mounted in the spectrometer where it's operating steadily with ArCO₂ gas mixture and nominal HV.

3.3 Gas Flow System

Figure 3.11 shows the up-to-date drift chamber's gas flow chart after adopting all modifications and changes in both the NM4 experimental hall and the external gas shed.

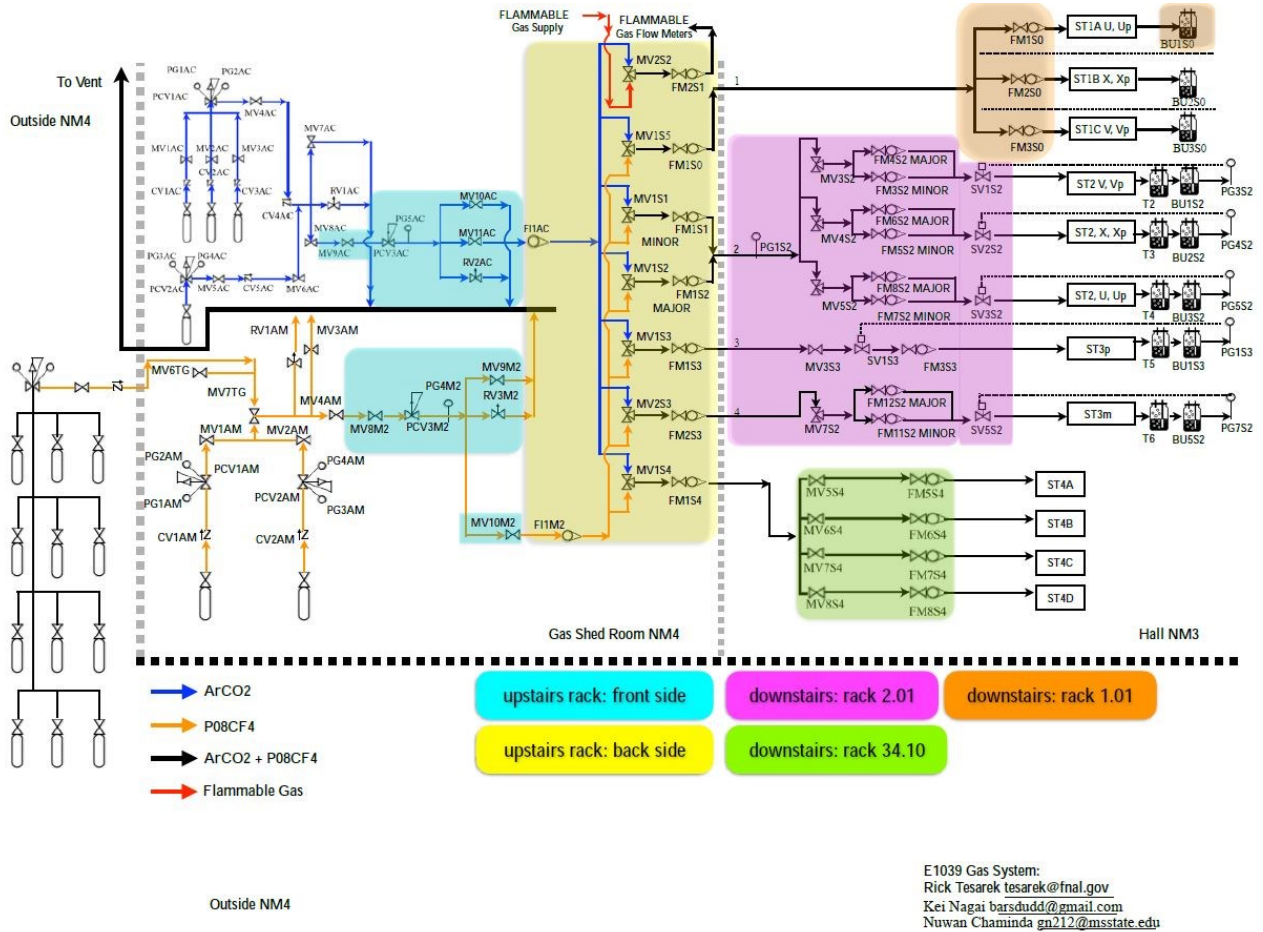


Figure 3.11 Gas flow chart from the external gas shed (left side) up to experimental hall flow meters racks (right side)

The gas volume is defined as $T \times W \times L$, where T is the chamber gas volume thickness, W is the chamber gas volume width, and L is the chamber gas volume length. The width and length are estimated based on the size of chamber's windows. However, the thickness is estimated by

examining the chamber's edges and considering the distance between its outermost planes. Figures 3.12 – 3.15 shows various DC dimensions in the three stations. For example, the D0 chambers structure consists of two outer windows (silver mylar), two inner cathode planes (gold mylar), two sense wires planes (gold tungsten wire; anode), and a central gold mylar cathode plane separating the prime and unprimed planes. The total distance between the two outer windows is about 1 inch.

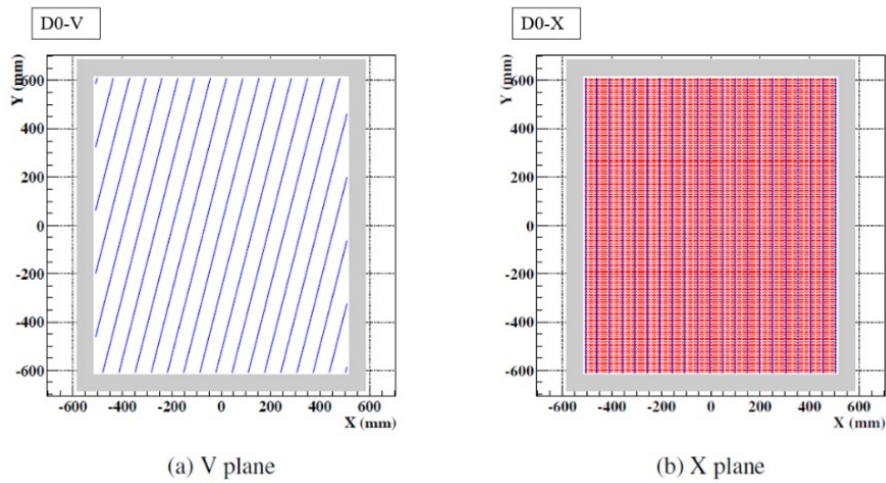


Figure 3.12 Some St-1 DC planes dimensions

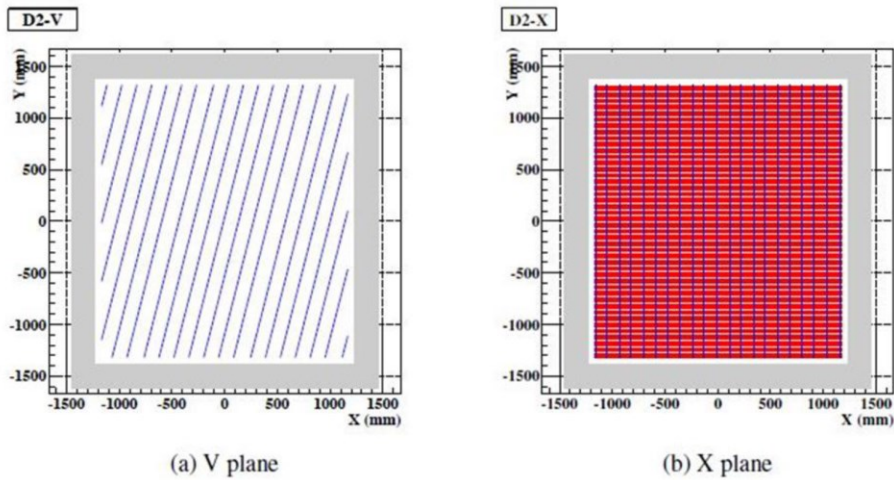


Figure 3.13 Some St-2 DC plane's dimensions

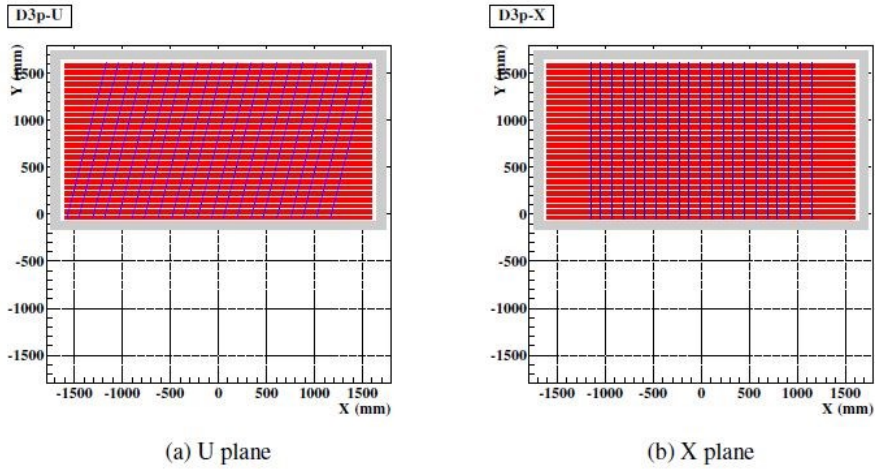


Figure 3.14 Some St-3 top-half DC plane's dimensions

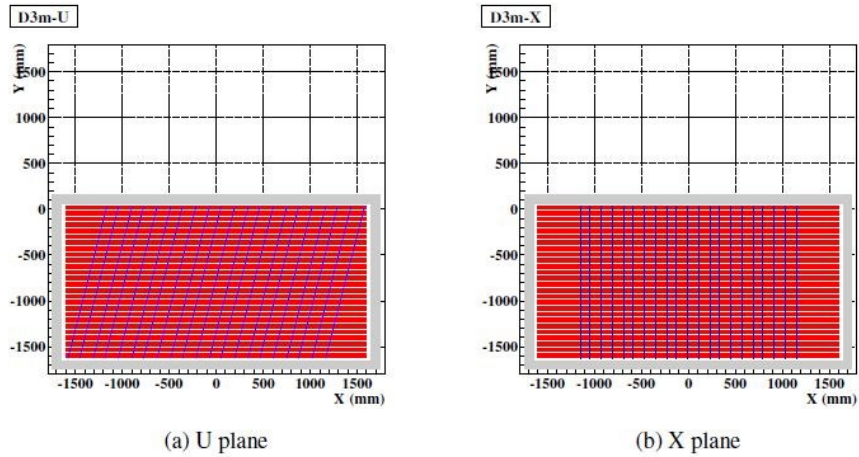


Figure 3.15 Some St-3 bottom-half DC plane's dimensions

In the process of exchanging gas mixtures or purging the drift chamber with gas after being opened/unused, the latter needs to be flushed at a maximum flow rate to kick out any air or old gas prior to data-taking. To determine the flushing time as well as rate, the total number of each chamber gas volumes should be found. The procedure described next is followed to obtain this information.

The variables as well as notations adopted in this calculation are; V is the total gas volume, $D(t)$ is the density of gas at time t , R is the gas flow rate, and n is the number of exchanged gas volumes.

Given the change of gas volume in a short time dt is equivalent to *the total gas volume inside* $\times dD = V \times dD$, then the change of a gas volume in a short time dt is *(inflow) – (outflow) = $Rdt - RDdt$.*

Therefore,

$$VdD = Rdt - RDdt$$

$$VdD = (1 - D)Rdt$$

$$\frac{dD(t)}{dt} = \frac{(1 - D)R}{V}$$

$$\frac{dD(t)}{dt} + \frac{R}{V}D = \frac{R}{V}$$

Multiply by $\int e^{\frac{R}{V}t}$ and integrating;

$$\int_0^t \frac{dD(t)}{dt} e^{\frac{R}{V}t} dt + \frac{R}{V} e^{\frac{R}{V}t} D dt = \int_0^t \frac{R}{V} e^{\frac{R}{V}t} dt$$

$$De^{\frac{R}{V}t} = \frac{R}{V} \int_0^t e^{\frac{R}{V}t} dt$$

$$De^{\frac{R}{V}t} = \frac{R}{V} \times \frac{V}{R} e^{\frac{R}{V}t} + C, \text{ where } C \text{ is a constant}$$

At $t = 0$;

$$0 = 1 + C$$

$$C = -1$$

Therefore,

$$D(t) = 1 - e^{-\frac{R}{V}t} \quad (3.1)$$

That's,

$$nV = Rt, \text{ or } t = \frac{nV}{R} \quad (3.2)$$

Substituting the value of t from equation 3.2 into equation 3.1 gives,

$$D(t) = 1 - e^{-\frac{R}{V} \times \frac{nV}{R}}$$

Therefore,

$$D(t) = 1 - e^{-n} \text{ or } D(t) = 1 - \frac{1}{e^n} \quad (3.3)$$

Equation 3.3 gives the relation between the exchanged gas volumes and the gas purity. For example, in case the number of gas volumes is three (five), the purity of gas inside the chamber is approximately 95% (99.3%). Table 3.4 shows the flushing time for each chamber which is obtained using Eq. 3.2.

Table 3.4 Running and flushing flow rates for various drift chambers

Chamber	Chamber dimensions			Volume (ft ³)	Number of volumes (n)	Flushing flow rate (SCFH)	Flushing time (t)		Purity of gas (%)	Running flow rate (SCFH)
	Length (ft)	Width (ft)	Height (ft)				In hours	In days		
D0VVp	3.93	0.25	3.93	3.86	5	0.42	46.0	1.91	99.3	0.42
D0XXp										
D0UUp										
D2VVp	10.6	0.57	11.4	68.88	5	2.10	164	6.83	99.3	0.90
D2XXp										
D2UUp										
D3p	11.15	0.93	5.58	57.86	5	2.70	107.1	4.46	99.3	2.70
D3m	11.15	0.93	5.58	57.86	5	1.80	160.7	6.70	99.3	1.60

The gas flow rates for operating and flushing different drift chambers depends mainly on their size. According to table 3.4, it is clear that D2 chambers takes the longest time to flush. Therefore, based on the D2 chambers scenario, the flushing flow rate was determined by checking the highest flow rate with the vent opened. Then, the operating flow rate was determined by checking the lowest flow rate with the vent closed. In both cases the pressure meters as well as bubblers were monitored to make sure that the chambers are not over pressurized. For example, D2UUp pressure is ~ 0.05 inches of water, which should remain constant in this procedure. After closing the vent lines on D2 chambers, their gas leak rates were also measured. In general, the leak rate is defined as "chamber gas volume" * "pressure decrease" / "atmosphere pressure" / "measurement time". To measure the D2 leak rates, the inflow was momentarily stopped, and the finding was as follows

- i. D2UUp leak rate = 0.352 ml/min (or 0.000739 SCFH)
- ii. D2XXp leak rate = 0.332 ml/min (or 0.000696 SCFH)
- iii. D2VVp leak rate = 0.405 ml/min (or 0.000851 SCFH)

Based on this method, flushing and operating flow rates and times were determined for all other drift chambers. Subsequently, all gas lines were cleaned and made ready to switch to the production gas mixture, P08:CF₄, a month or so prior to the upcoming beam commissioning in fall 2022. The NM4 gas shed is already packed with a dozen of a production gas cylinders which are equipped with new pressure regulators for an easy switch during the upcoming run period.

CHAPTER IV
DRIFT CHAMBERS STUDIES

4.1 Chamber Efficiency

This study was performed mainly for St-2 and St-3 drift chambers given some St-1 D0 chambers were still under debugging and/or repair. To achieve the overall tracking performance, each DC plane efficiency is supposed to be in the range of 95% which implies that all chambers are operating at their HV nominals as reducing it will make related planes less efficient. The in-plane efficiency is defined as

$$iEff = \frac{N_{12}}{N_{12} + N_{11}} \quad (4.1)$$

where N_{12} is the number of the track-associated hits in the twelve planes of St-2 and St-3 DC, and N_{11} is the number of hits without the target plane. For example, if we are interested to extract the in-plane efficiency of the target plane D2X, then N_{11} will contain hits from all other D2 and D3p/m planes except D2X, assumed as inefficient in this case. Two sets of cuts are applied in this study to select good tracks: 1) number of hits higher than or equal to eleven, and 2) reduced χ^2 (redChisq) defined as

$$\tilde{\chi}^2 = \frac{\chi^2}{d} \quad (4.2)$$

where d is the number of degrees of freedom and χ^2 is

$$\chi^2 = \sum_1^n \frac{(Observed - Expected)^2}{Expected} \quad (4.3)$$

is less than 1 while "Observed" is the calculated efficiency and "Expected" is at least 95% in-plane efficiency. In this case, the utilized tracklets are the reconstructed back partial track between St-2 and St-3 chambers. For a good fit the expected value of the redChisq should be one since most data falls into ± 1 sigma region.

4.1.1 Statistical Uncertainty Calculation

This uncertainty is evaluated using the Bayesian probability calculation. In this Bayesian method, effects are considered a result of causes, where effects, in our case, are a specific detector configuration and causes are the underlying physics distribution. [12]

$$Error = \frac{(A + 1)(B + 1)}{(A + B + 2)^2(A + B + 3)} \quad (4.4)$$

where $A = N_{12}$ and $B = N_{11}$ as defined in Eq. 4.1.

The results of in-plane efficiency and its error calculation is summarized in Table 4.1 for a cosmic ray run # 2155 taken back in 2020. In this run, the DC HV for D2 and D3p/m were set at 2.0 kV, and 2.48 kV, respectively. It's worth noting that this run was taken before the D2UUp repair that was described in Ch.3, thus the results at least for this chamber is not necessary reflecting the current chamber conditions.

Table 4.1 In-plane efficiencies and their uncertainties for St-2 and St-3 DC extracted for a cosmic ray run # 2155 taken on November 2020. The evaluation was done with 10176 tracklets, out of which 3094 have a number of hits higher than 11 are 3094 and 2711 have RedChisq < 1

Detector ID	Plane	# of efficient tracks	# of inefficient tracks	Efficiency (%)	Error
13	D2V	652	372	63.67	± 1.50
14	D2Vp	652	335	66.06	± 1.51
15	D2Xp	652	271	70.64	± 1.50
16	D2X	652	274	70.41	± 1.50
17	D2U	652	243	72.85	± 1.48
18	D2Up	652	268	70.87	± 1.50
19	D3pVp	118	11	91.47	± 2.51
20	D3pV	118	7	94.40	± 2.15
21	D3pXp	118	3	97.52	± 1.59
22	D3pX	118	9	92.91	± 2.35
23	D3pUp	118	8	93.65	± 2.25
24	D3pU	118	11	91.47	± 2.51
25	D3mVp	534	34	94.01	± 1.00
26	D3mV	534	35	93.84	± 1.01
27	D3mXp	534	46	92.07	± 1.11
28	D3mX	534	55	90.66	± 1.20
29	D3mUp	534	39	93.19	± 1.06
30	D3mU	534	38	93.36	± 1.05

4.2 Extraction of Calibration Parameters

Drift chambers calibration, the so-called RT curve, is needed to determine the correlation between the drift time (T) obtained from the TDC time (t) and the drift distance (R). The described effort in this section focuses on extracting the allowable range of some variables that are fed to the routine calculating the RT curve. The concerned variables are

- i. x_0 , the x-position of track at the reference plane $z = 0$ cm,
- ii. y_0 , the y- position at reference plane $z=0$ cm,

- iii. t_x , the slope in the x-direction at the z-position of a specific drift chamber plane,
- iv. t_y , the slope in y-direction at a z-position of a specific drift chamber plane,
- v. x_z , the x-position at a specific z-position of a drift chamber, and
- vi. y_z , the y-position at a specific z-position of a drift chamber.

An illustration of hands-on extraction of some of these variables especially x_z and y_z at $z=1900$ cm, which is the z-position of D3mU plane, is depicted in Figs 4.1 and 4.2, respectively, using two cosmic tracks crossing the plane.

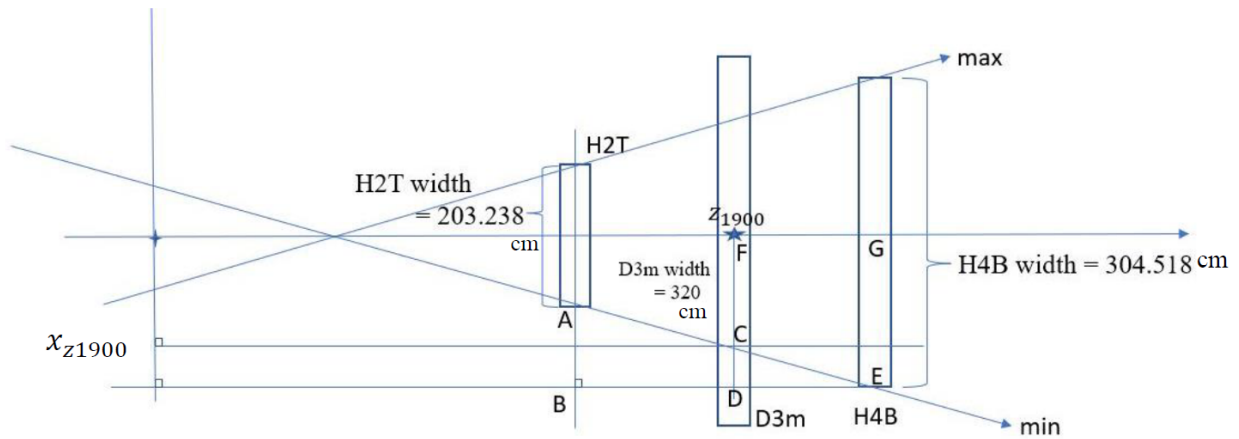


Figure 4.1 The sketch of the x_z extraction at $z=1900$ cm corresponding to u plane of D3m chamber

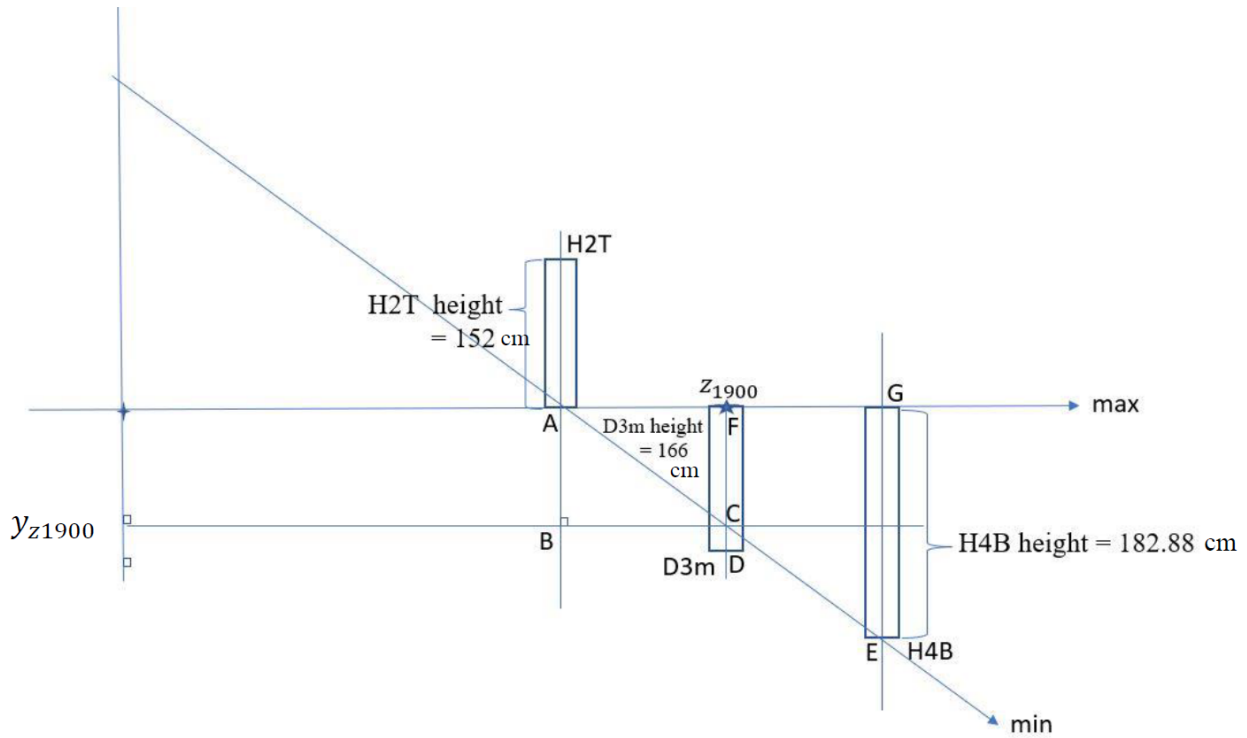


Figure 4.2 The sketch of the y_z extraction at $z = 1900$ cm corresponding to u plane of D3m chamber

Before start looking to the current E1039 cosmic ray data, some work was done to understand and run the calibration scripts developed for the previous E906 experiment to extract the parameters mentioned above. For illustration only, the calibration figures shown here are for the D3pX plane. The extraction performed here is based on the definition of the following quantities: the drift distance (R), the track distance (D), representing the distance from the track to the sense wire, and the residual ($\equiv R - D$), which is the single-plane resolution averaged over R . Figures 4.3 and 4.4 show the drift and track distance distributions, while Fig 4.5 illustrates their 2D correlation. Figure 4.6 shows the dependence of the residual on the TDC time which is centered around zero as an indication of successfully performing the calibration procedure. Figure 4.7 shows the final calibration results of this E906 data test in terms of the obtained D3pX RT curve,

while Fig. 4,8 illustrates the 2D dependence between the drift time and the signed R, which is the drift distance with an assigned +/- sign depending on the reconstructed track direction.

Table 4.2 Station IDs for each drift chamber

Type	Station ID
D0 tracklet	1
D1 tracklet	2
D2 tracklet	3
D3p tracklet	4
D3m tracklet	5
D2+3 tracklet	6
Global track	7

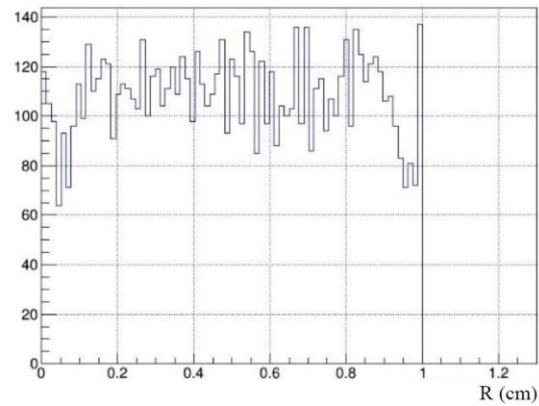


Figure 4.3 Drift distance distribution

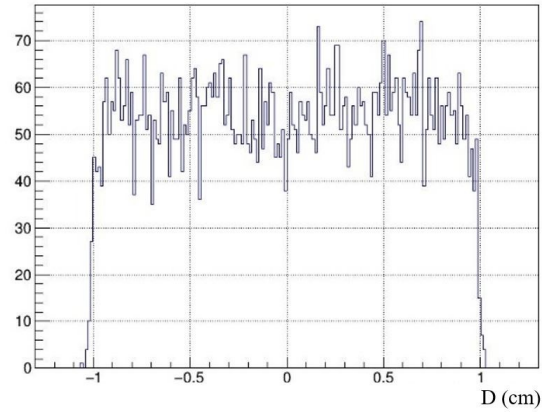


Figure 4.4 Track distance distribution

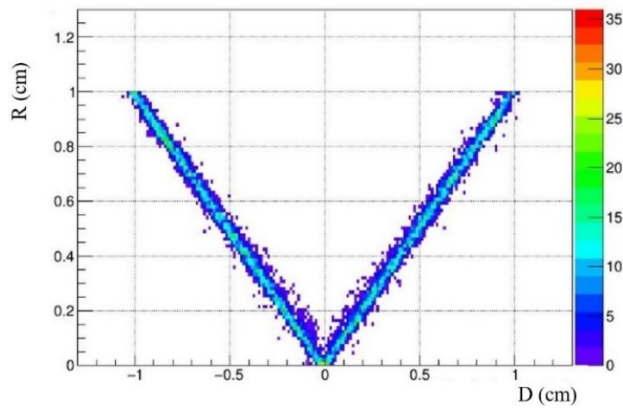


Figure 4.5 Drift distance, R , as a function of track distance, D

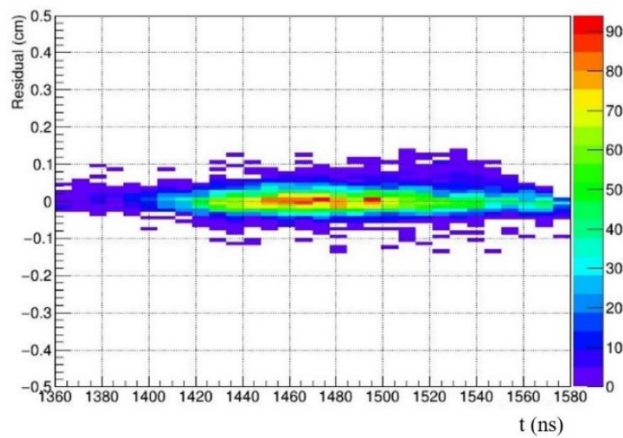


Figure 4.6 Residual and TDC time, t , correlation

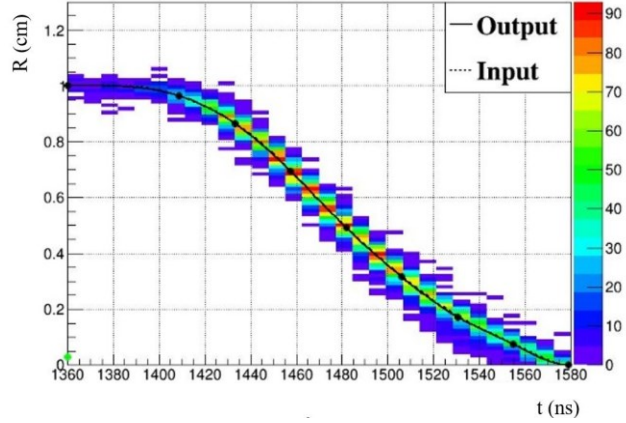


Figure 4.7 Illustration of the extracted RT curve in terms of the drift distance, R, and the TDC time, t (ns) correlation

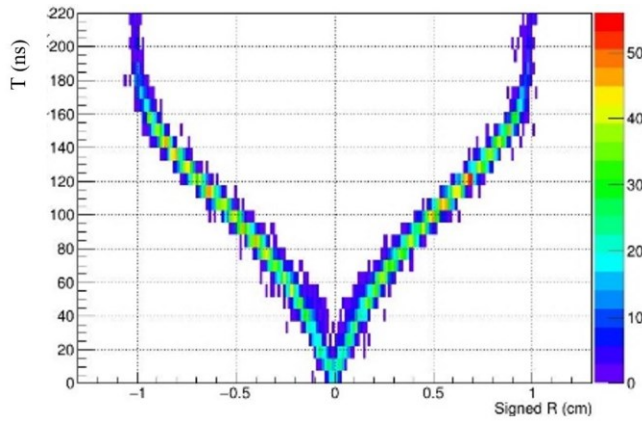


Figure 4.8 Drift time, T, as a function of signed drift distance, R

After learning how to run the E906 calibration scripts, the latter were used to process some E1039/SpinQuest cosmic rays data to extract the allowable ranges of variables mentioned above. The finding for different stations is listed below.

1. D3m chamber: For example, the calculation based on Fig. 4.1 notation is as follows:

The maximum of x_{z1900} is equivalent to FC, which is $\underline{FC} \equiv GE - CD = GE - DE \times \tan(A\hat{E}B)$.

With the known geometry of hodoscopes and chambers at various stations, all these values can be

calculated. All other allowable ranges were found using a similar geometrical approach. The obtained allowable ranges for $x_0, y_0, t_x, t_y, x_{z1900},$ and y_{z1900} are

x_0 [- 535.89960336 cm, 535.89960336 cm]; x position at $z = 0$ cm

y_0 [- 724.84059375 cm, 724.84059375 cm]; y position at $z = 0$ cm

t_x [- 0.305616, 0.305616]; x slope at $z = 1900$ cm

t_y [- 0.403125, 0.403125]; y slope at $z = 1900$ cm

x_{z1900} [-130.82 cm, 130.82 cm]; x position at $z = 1900$ cm

y_{z1900} [-169.807 cm, 0 cm]; y position at $z = 1900$ cm

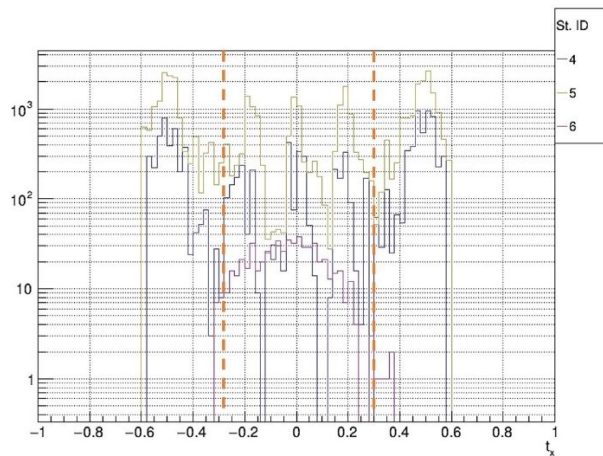


Figure 4.9 t_x distribution for D3mU plane with the allowable range shown with dashed red lines

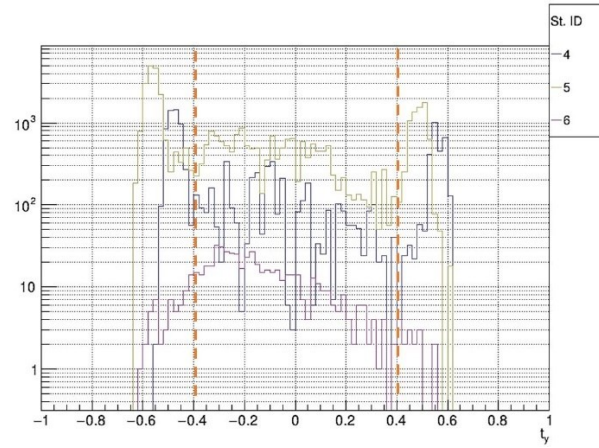


Figure 4.10 t_y distribution for D3mU plane with the allowable range shown with dashed red lines

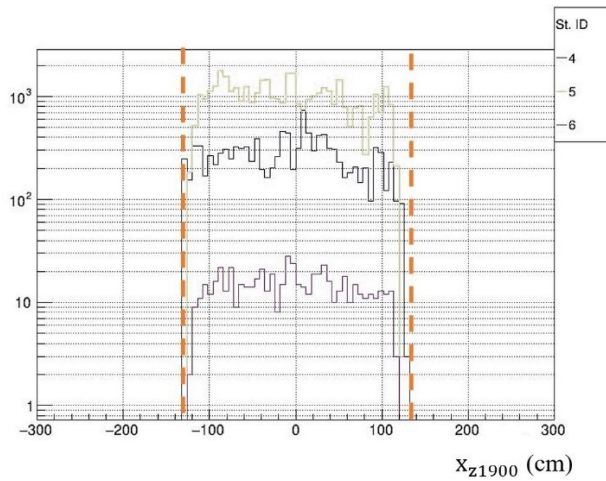


Figure 4.11 The x-position distribution at $z=1900$ cm, corresponding to D3mU plane with the allowable range shown with dashed red lines

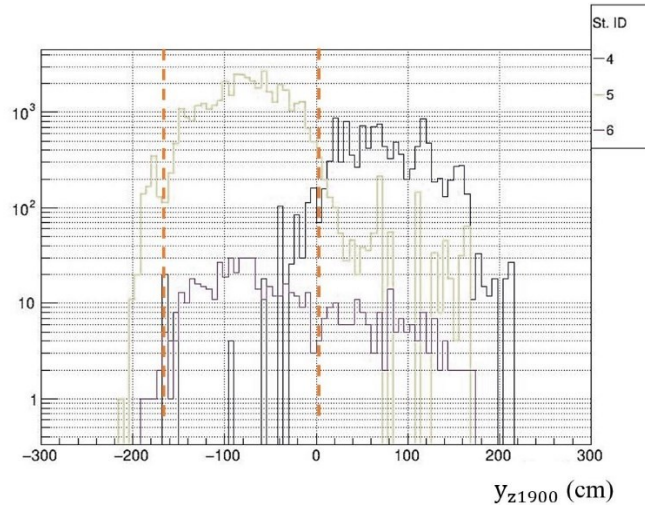


Figure 4.12 The y-position distribution at z= 1900 cm, corresponding to D3mU plane with the allowable range shown with dashed red lines

Figures 4.9 - 4.12 show the t_x , t_y , x_z , and y_z distributions for the u plane of D3m chamber with their allowable ranges marked with the red dashed lines.

2. D3pXXp chamber: The obtained allowable ranges for x_0 , y_0 , t_x , t_y , x_{z1937} , and y_{z1937} are

$$x_0 [-535.89960336 \text{ cm}, 535.89960336 \text{ cm}]; \text{ x position at } z = 0 \text{ cm}$$

$$y_0 [0 \text{ cm}, 724.84059375 \text{ cm}]; \text{ y position at } z = 0 \text{ cm}$$

$$t_x [-0.305616, 0.305616]; \text{ x slope at } z = 1937 \text{ cm}$$

$$t_y [0, 0.403125]; \text{ y slope at } z = 1937 \text{ cm}$$

$$x_{z1937}[-285.33\text{cm}, 285.33 \text{ cm}]; \text{ x position at } z = 1937 \text{ cm}$$

$$y_{z1937} [0 \text{ cm}, 113.57 \text{ cm}]; \text{ y position at } z = 1937 \text{ cm}$$

3. D2XXp chamber: The obtained allowable ranges for x_0 , y_0 , t_x , t_y , x_{z1347} , and y_{z1347} are

$$x_0 [-243.669 \text{ cm}, 243.669 \text{ cm}]; \text{ x position at } z = 0 \text{ cm}$$

$$y_0 [-267.45449 \text{ cm}, 267.45449 \text{ cm}]; \text{ y position at } z = 0 \text{ cm}$$

t_x [-0.242998, 0.242998]; x slope at $z = 1347$ cm

t_y [-0.295193, 0.295193]; y slope at $z = 1347$ cm

x_{z1347} [-101.05 cm, 101.05 cm]; x position at $z = 1347$ cm

y_{z1347} [-137.11 cm, 0 cm]; y position at $z = 1347$ cm

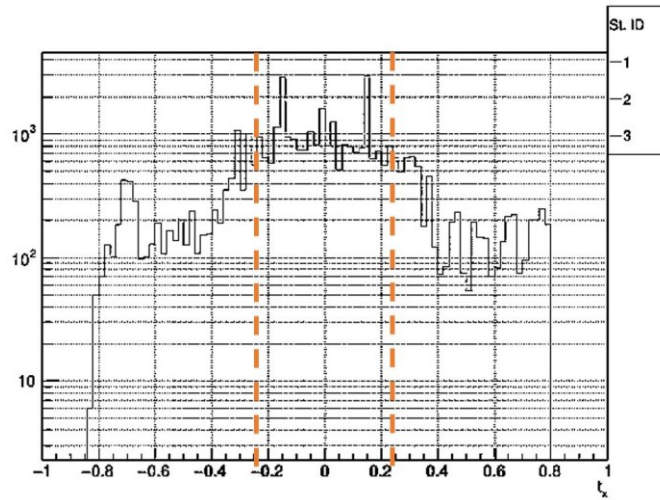


Figure 4.13 t_x distribution for D2X plane with the allowable range shown with dashed red lines

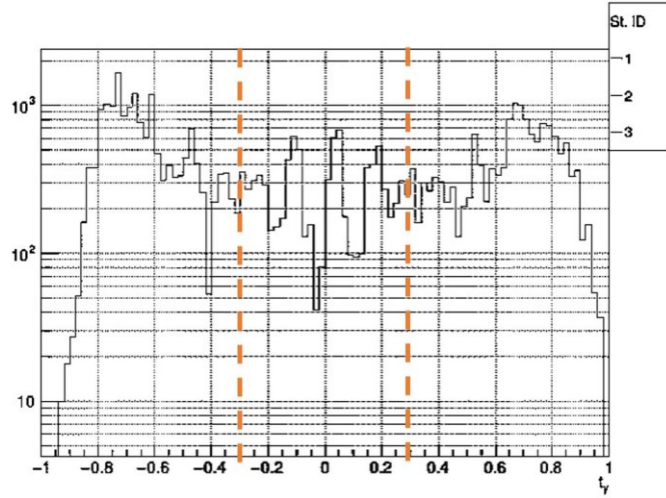


Figure 4.14 t_y distribution for D2X plane with the allowable range shown with dashed red lines

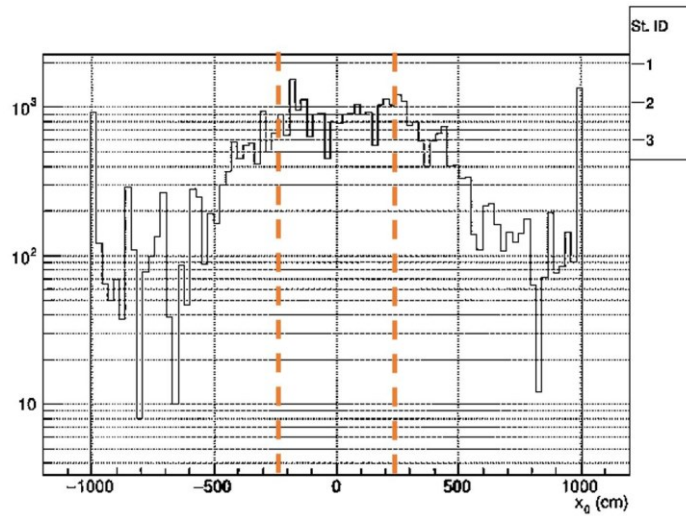


Figure 4.15 x_0 distribution for D2X plane with the allowable range shown with dashed red lines

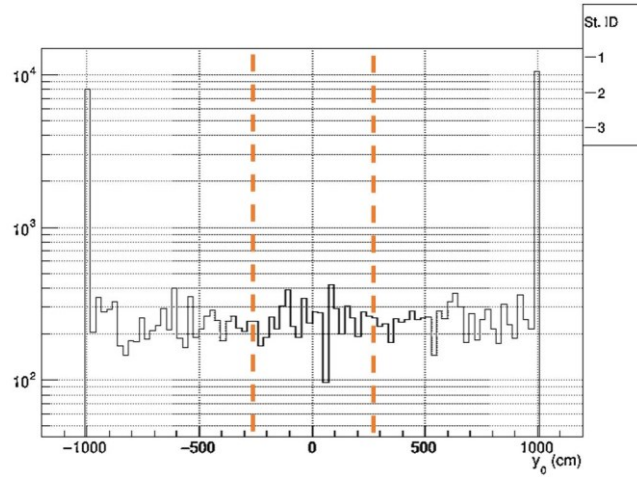


Figure 4.16 y_0 distribution for D2X plane with the allowable range shown with dashed red lines

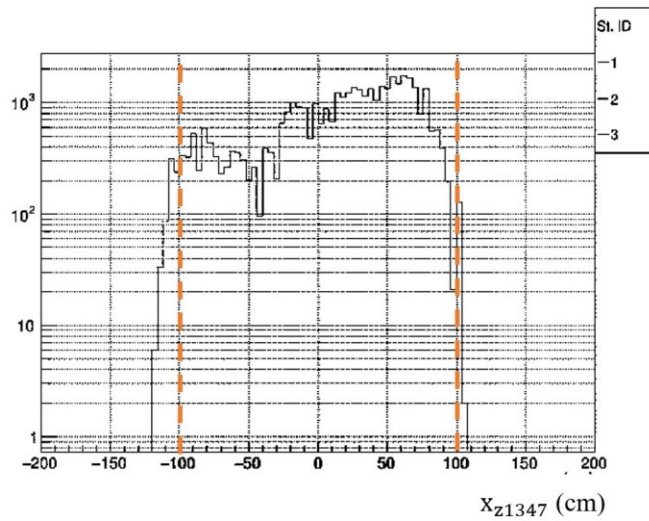


Figure 4.17 The x-position distribution at $z=1347$ cm, corresponding to D2X plane with the allowable range shown with dashed red lines

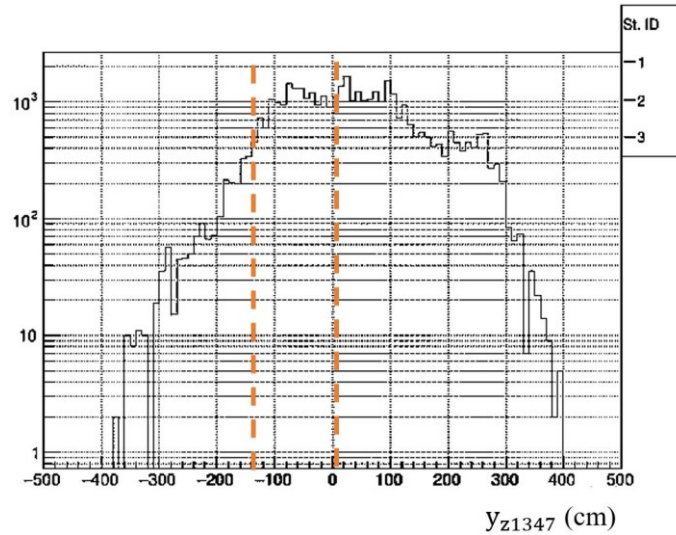


Figure 4.18 The y-position distribution at $z=1347$ cm, corresponding to D2X plane with the allowable range shown with dashed red lines

Figures 4.13 - 4.18 show the $x_0, y_0, t_x, t_y, x_z,$ and y_z distributions for the u plane of D3m chamber with their allowable ranges marked with the red dashed lines.

4. DOUUp chamber: The obtained allowable ranges for $x_0, y_0, t_x, t_y, x_{z649},$ and y_{z649} are

x_0 [-161.683 cm, 161.683 cm]; x position at $z = 0$ cm

y_0 [-215.742 cm, 215.742 cm]; y position at $z = 0$ cm

t_x [-0.1853, 0.1853]; x slope at $z = 649$ cm

t_y [-0.2588, 0.2588]; y slope at $z = 649$ cm

x_{z649} [-101.6 cm, 101.6 cm]; x position at $z = 649$ cm

y_{z649} [-4.128 cm, 4.128 cm]; y position at $z = 649$ cm

The conclusion of this study is being able to determine the appropriate range of sensitive calibration parameters that are fed to the analysis scripts to extract the RT curves for the E1039 data. For example, the following cuts were adopted to select good tracks for D3m chamber:

x_0 [- 536 cm, 536 cm]; x position at $z = 0$ cm

y_0 [- 725 cm, 725 cm]; y position at $z = 0$ cm

t_x [- 0.3, 0.3]; x slope at $z = 1900$ cm

t_y [- 0.4, 0.4]; y slope at $z = 1900$ cm

x_{z1900} [-131 cm, 131 cm]; x position at $z = 1900$ cm

y_{z1900} [-170 cm, 0 cm]; y position at $z = 1900$ cm

CHAPTER V

SUMMARY AND OUTLOOK

In summary, all stations drift chambers are debugged, refurbished as needed, and tested as a preparation for the upcoming beam commissioning in fall 2022. Any remaining inefficient, noisy or dead wires are internal and are left as is. However, there are still some ongoing efforts by the DC group members to fix an/or reduce the noise level of some chambers. This work is expected to conclude at most by late summer. Furthermore, a new efficiency study will be performed to extract the in-plane efficiencies for all chambers, D0, D2, and D3p/m, with both ArCO₂ and P8CF₄ gas mixtures based on cosmic ray data. As reported, the gas flow system was updated and made ready to switch to the production gas, P8CF₄, that the SpinQuest experiment intends to use.

It's anticipated that after a successful polarized target commissioning, the whole E1039 spectrometer will be commissioned with the 120 GeV proton beam. To this end, a HV scan will be performed again and the in-plane efficiencies will be evaluated to determine the HV nominals for DC planes. Typically, such a measurement relies on using a clean data sample provided by a single muon trigger and low intensity beam with either KMAG ON or OFF. The latter is needed specifically for the spectrometer alignment with a straight tracks. In parallel, the chamber's TDC time windows can be adjusted leading to the RT curves extraction. Our group is leading the online reconstruction efforts with graphical processing units (GPU) which will allow monitoring and displaying the spectrometer performance as well as reconstructed physics variables on real time.

A successful completion of all commissioning tasks will lead the E1039/SpinQuest collaboration to focus on fulfilling the project physics goals during the production mode, starting from the "Day-one" physics that was highlighted in the introduction chapter.

REFERENCES

- [1] C. Brown et al., “Letter of Intent for a Drell-Yan Experiment with a Polarized Proton Target”, FERMILAB-PROPOSAL-1039, 2014
- [2] A. Adare et al. (PHENIX Collaboration), “Measurement of Transverse Single-Spin Asymmetries for J/ψ Production in Polarized $p + p$ Collisions at $\sqrt{s} = 200$ GeV”, Phys. Rev. D 82: 112008, 2011.
- [3] P.P. Bhaduri, A. K. Chaudhuri, and S. Chattopadhyay, “ J/ψ production in proton-induced collisions at energies available at the GSI Facility for Antiproton and Ion Research”, Phys. Rev. C 84, 20
- [4] Dove, J., Kerns, B., McClellan, R.E. et al. The asymmetry of antimatter in the proton. Nature 590, 561–565 (2021). <https://doi.org/10.1038/s41586-021-03282-z>
- [5] SeaQuest spectrometer at Fermilab, Nuclear Instruments and Methods in Physics Research Section A: Accelerators, Spectrometers, Detectors and Associated Equipment, Volume 930, 2019, ISSN 0168-9002, <https://doi.org/10.1016/j.nima.2019.03.039>
- [6] Kei Nagai, Recent Measurement of Flavor Asymmetry of Antiquarks in the Proton by Drell–Yan Experiment SeaQuest at Fermilab, PhD Thesis, 2017, <https://seaquest-docdb.fnal.gov/cgi-bin/sso/ShowDocument?docid=2204>
- [7] Jason Dove, Probing the Flavor Dependence of Proton's Light-Quark Sea in the Seaquest Experiment at Fermilab, PhD Thesis, 2020, <https://seaquest-docdb.fnal.gov/cgi-bin/sso/ShowDocument?docid=8315>
- [8] The SpinQuest polarized target, <https://spinquest.fnal.gov/polarized-target/>
- [9] Bryan Kerns, A measurement of the x dependent sea flavor asymmetry at SeaQuest, 2018, <https://seaquest-docdb.fnal.gov/cgi-bin/sso/ShowDocument?docid=3120>
- [10] E. Garutti, Gaseous detectors- measurement of ionization position determination, https://www.desy.de/~garutti/LECTURES/ParticleDetectorSS12/L4_gasDetectors.pdf, [Online; accessed January 21, 2020].

- [11] David C Christian, Level Shifter Command Summary, SEAQUEST Document 363-v2, <https://seaquest-docdb.fnal.gov/cgi-bin/sso/ShowDocument?docid=363>
- [12] TEfficiency - a class to handle efficiency histograms, <https://root.cern/root/html534/TEfficiency.html>